

1 **Histology-Compatible MALDI Mass Spectrometry Based Imaging of**  
2 **Neuronal Lipids for Subsequent Immunofluorescent Staining:**

3

4 *Ibrahim Kaya*<sup>1</sup>, *Wojciech Michno*<sup>1</sup>, *Dimitri Brinet*<sup>1,2</sup>, *Yasmine Iacone*<sup>1</sup>, *Giulia Zanni*<sup>3</sup>,  
5 *Kaj Blennow*<sup>1,4</sup>, *Henrik Zetterberg*<sup>1,4,5</sup>, *Jörg Hanrieder*<sup>1,4,5,6</sup>

6

7 <sup>1</sup> Department of Psychiatry and Neurochemistry, Sahlgrenska Academy at the University of  
8 Gothenburg, Mölndal, Sweden

9 <sup>2</sup> Department of Chemistry and Molecular Biology, University of Gothenburg, Sweden

10 <sup>3</sup> Karolinska Institute, Department of Women's and Children's Health, Karolinska University  
11 Hospital, Stockholm, Sweden

12 <sup>4</sup> Clinical Neurochemistry Laboratory, Sahlgrenska University Hospital, Mölndal, Sweden.

13 <sup>5</sup> Department of Molecular Neuroscience, Institute of Neurology, University College London,  
14 UK

15 <sup>6</sup> Department of Chemistry and Chemical Engineering, Chalmers University of Technology,  
16 Gothenburg, Sweden

17

18 **Corresponding Author**

19 Jörg Hanrieder, PhD

20 Department of Psychiatry and Neurochemistry, Sahlgrenska Academy at the University of  
21 Gothenburg, Mölndal Hospital, House V, Biskopsbogatan 27, SE-43180 Mölndal, Sweden

22 [jh@gu.se](mailto:jh@gu.se); +46-31-343 2377

23

24

## 25 **ABSTRACT**

26 Matrix assisted laser desorption/ionization imaging mass spectrometry (MALDI-IMS)  
27 enables acquisition of spatial distribution maps for molecular species in situ. This can  
28 provide comprehensive insights on the pathophysiology of different diseases. However,  
29 current sample preparation and MALDI-IMS acquisition methods have limitations in  
30 preserving molecular and histological tissue morphology, resulting in interfered  
31 correspondence of MALDI-IMS data with subsequently acquired immunofluorescent staining  
32 results. We here investigated the histology-compatibility of MALDI-IMS paradigm to image  
33 neuronal lipids in rodent brain tissue with subsequent immunohistochemistry and fluorescent  
34 staining of histological features. This was achieved by sublimation of a low ionization energy  
35 matrix compound, 1,5-diaminonaphthalene (1,5-DAN), minimizing the number of low-energy  
36 laser shots. This yielded improved lipid spectral quality, speed of data acquisition and  
37 reduced matrix cluster formation along with preservation of specific histological information  
38 at cellular levels. The gentle, histology compatible MALDI IMS protocol also diminished  
39 thermal effects and mechanical stress created during nanosecond laser ablation processes  
40 that resulted in subsequent immuno fluorescence staining but not with classical H&E  
41 staining on the same tissue section. Furthermore, this methodology proved to be a powerful  
42 strategy for investigating  $\beta$ -amyloid ( $A\beta$ ) plaque-associated neuronal lipids as exemplified by  
43 performing high-resolution MALDI-IMS with subsequent fluorescent amyloid staining in a  
44 transgenic mouse model of Alzheimer's disease (tgSwe).

45

46 **Keywords:** MALDI imaging mass spectrometry (IMS), immunohistochemistry, histology,  
47 tissue integrity, laser ablation on biological tissues, Alzheimer's disease (AD), amyloid beta  
48 ( $A\beta$ ) plaques, Amyloid- $\beta$  Plaque Associated Neuronal Lipids

49

## 50 INTRODUCTION

51 Lipids are the most abundant components of neural cell membranes, having a variety of  
52 functions in neurobiological processes including metabolism, cell adhesion and migration,  
53 signal transduction, and apoptosis.<sup>1-3</sup> Moreover, they may play roles in the pathogenesis of  
54 many neurodegenerative diseases, such as in Alzheimer's disease<sup>4</sup>, Parkinson's disease<sup>5</sup>,  
55 amyotrophic lateral sclerosis (ALS)<sup>6</sup> and multiple sclerosis (MS)<sup>7</sup>, which all show lipid  
56 alterations in the central nervous system.<sup>4, 5, 8</sup> Therefore, to investigate the spatial distribution  
57 of neuronal lipids and to disentangle their functional roles *in situ*, advanced chemical imaging  
58 techniques, such as imaging mass spectrometry (IMS), are required.<sup>9, 10</sup>

59 IMS allows for examining the molecular architecture in complex biological matrices and  
60 hence often referred to as molecular histology.<sup>11</sup> The technique can be used for spatial  
61 mapping of neuronal molecules in mammalian brain tissue<sup>10, 12, 13</sup>, which can be employed in  
62 the study of neurodegenerative diseases.<sup>14, 15</sup> MALDI-IMS has been several times  
63 demonstrated to be an effective tool for probing of neuronal lipids<sup>11, 14</sup>, peptides<sup>16, 17</sup> and  
64 proteins *in-situ*.<sup>9, 18</sup> For MALDI-IMS, a desorption enhancing photon-absorbing matrix  
65 compound<sup>19</sup> is applied onto tissue section

66 Many sample preparation methods have been developed for improving MALDI-IMS  
67 performance in order to enhance the analyte signal-to-noise (S/N) ratio, minimize analyte  
68 delocalization and provide high spatial resolution for lipid molecular species in different tissue  
69 types.<sup>20, 21</sup> In these studies, homogeneous matrix coating has been addressed as a crucial  
70 step in terms of high spatial resolution. It has been concluded that most matrix coating  
71 methods including use of solvents have a risk of analyte delocalization, in particular for small  
72 molecules (e.g. lipids). Therefore, dry matrix coating strategies have been developed for  
73 high-spatial resolution analysis. Sublimation is a solvent-free, dry approach for matrix  
74 application in MALDI-IMS<sup>21</sup> and was demonstrated to give the best data in terms of signal

75 quality and ion image resolution for lipid molecules allowing improved correlation with  
76 histological information.<sup>20, 22</sup>

77 In most MALDI imaging studies, histological staining with e.g. hematoxylin and eosin (H&E)  
78 is commonly performed following the MALDI-IMS analysis on the same tissue section in  
79 order to correlate ion image data with histological features.<sup>23, 24</sup> While H&E staining is a  
80 histological staining technique to evaluate cell and tissue structures, it is not specific to  
81 distinct protein epitopes as immunohistochemistry (IHC). However, IHC and fluorescent  
82 staining following MALDI-IMS analysis on the same tissue sections can be challenging due  
83 to the potential tissue distortion and epitope degradation as a consequence of laser  
84 ablation.<sup>25</sup> Here, mechanical stress along with thermal denaturation effects induced by  
85 nanosecond pulse laser ablation<sup>25, 26</sup> is likely to impact the morphology, integrity and  
86 molecular composition of histological tissue section. Consequently, this can impair accurate  
87 correlation between MALDI-IMS and histological staining data. As a result, the laser ablation  
88 process on biological tissues should be taken into consideration for efficient multimodal  
89 imaging analysis schemes, as this can be a major reason for inconclusive correlations.  
90 Currently, there are only few reports on subsequent immunofluorescent staining following  
91 MALDI-IMS analysis on the same tissue section, with in part inconclusive IMS/IHC  
92 correlation results.<sup>14, 17, 27</sup> We previously studied amyloid-plaque associated neuronal lipids  
93 and amyloid- $\beta$  peptide species in transgenic Alzheimer's disease (AD) mice using MALDI-  
94 IMS of lipids<sup>14</sup> and peptides<sup>17</sup> followed by immunofluorescent staining of plaques on the  
95 same section. Although co-localization of MALDI ion images and fluorescent amyloid images  
96 was obtained in these studies for qualitative validation, the IMS/IHC signal alignment was not  
97 optimal at higher resolution scales.<sup>14, 17</sup> This was particularly prominent for peptide imaging  
98 as these MALDI experiments require higher laser pulse energies for desorption-ionization of  
99 large peptides and proteins.<sup>28</sup> Since, all of these studies employed a nanosecond Nd:YAG  
100 laser with structured beam profile,<sup>29</sup> it is relevant to consider the local mechanical and

101 thermal denaturation effects during laser ablation process to enhance MALDI-IMS  
102 compatibility for subsequent immunofluorescent staining.

103 The aim of the present study, was to therefore to investigate the histology compatibility of  
104 sublimation based matrix deposition for MALDI-IMS spatial profiling of neuronal lipids with  
105 subsequent multiplexed immunofluorescent staining in mice brain. Here, sublimation with  
106 1,5-diaminonaphthalene (1,5-DAN) as MALDI matrix was found to give the best lipid signals  
107 in both ionization modes using low laser pulse energies and number of laser shots. This  
108 further resulted in minimal damage in tissue integrity and morphology for follow up  
109 immunofluorescent staining on the same tissue. In addition, the final method was  
110 exemplified on a transgenic Alzheimer's disease mice model (tgSwe) to examine cortical A $\beta$   
111 plaque pathology-associated lipid profiles *in situ*.

112

## 113 **EXPERIMENTAL SECTION**

114 **Chemicals and Reagents.** All chemicals for matrix and solvent preparation were pro-  
115 analysis grade and obtained from Sigma-Aldrich (St. Louis, MO), unless otherwise specified.  
116 TissueTek optimal cutting temperature (OCT) compound was purchased from Sakura  
117 Finetek (AJ Alphen aan den Rijn, The Netherlands). The *d*<sub>4</sub>H<sub>2</sub>O was obtained from a MilliQ  
118 purification system (Merck Millipore, Darmstadt, Germany).

119

120 **Animals.** C57BL/6 female mice from Charles Rivers Laboratories were used for method  
121 development (Sulzfeld, Germany). The animals were housed at the animal facility in  
122 Gothenburg (Laboratory of Experimental Biomedicine, EBM), kept under standard conditions  
123 of daylight (12-hour light cycle) and provided with food and water *ad libitum*. Animals were  
124 delivered with their respective dams that were further separated at postnatal day (PND) 21 of  
125 the pups. For the analysis, animals were anesthetized with isoflurane and killed by  
126 decapitation.

127 Transgenic AD mice, 18 months of age, carrying the Swedish mutation (K670N, M671L) of  
128 human APP (tgSwe) were used and reared ad libitum at the animal facility at Uppsala  
129 University under a 12/12-hlight/dark cycle.<sup>30</sup> All experimental conditions were approved by  
130 the Animal Research Ethics Committee (Gothenburg committee of the Swedish Agricultural  
131 Agency and Uppsala University), in accordance with the national animal welfare legislation.  
132 The following ethical identification number was used: (DNr #20-2013, Gothenburg; DNr  
133 #C17/14, Uppsala University).

134  
135 **Tissue Sampling and Sectioning.** The brains were dissected quickly with 3 minutes  
136 postmortem delay and frozen on dry ice. Frozen tissue sections (12 $\mu$ m) were cut in a  
137 cryostat microtome (Leica CM 1520, Leica Biosystems, Nussloch, Germany) at 18°C, and  
138 collected on special-coated, conductive ITO (indium tin oxide) coated glass slides (Bruker  
139 Daltonics, Bremen, Germany) and stored at -80°C. Prior to matrix deposition by sublimation,  
140 tissue sections were thawed in a desiccator for 30 minutes under reduced pressure  
141 (SpeedVac, Eppendorf, Hamburg, Germany).

142  
143 **Sublimation based Matrix Deposition.** Matrix deposition was carried out in a sublimation  
144 apparatus (Sigma Aldrich) as previously described.<sup>14</sup> The sublimation protocol was  
145 optimized with respect to temperature, deposition time and total amount of deposited matrix  
146 in order to obtain the best detection efficiency for lipids on mice brain tissue. Under stable  
147 vacuum (0.8 mbar) and temperature (130°C) conditions, we varied the amount of matrix  
148 coating between 50 and 300 $\mu$ g/cm<sup>2</sup>. A too thin matrix layer (50-70 $\mu$ g/cm<sup>2</sup>) yielded very few  
149 lipid ions, while a too thick matrix layer (200-300 $\mu$ g/cm<sup>2</sup>) resulted in dominant matrix ions  
150 (Supporting Information, Figure S-1). With this setup, the optimum matrix layer was found to  
151 be 120 $\mu$ g/cm<sup>2</sup> to give the best lipid signals, which is in a good agreement with previous  
152 results<sup>31</sup>. We used optimized sublimation conditions: 20 minutes at a temperature of 130°C  
153 under a stable vacuum of 0.8 mbar. Homogeneity of the matrix distribution over the analyzed

154 sections was evaluated by monitoring the non-normalized ion intensity of a proposed matrix  
155 derived [2DAN-2H]<sup>+</sup> Ion.<sup>31</sup> (Supporting Information Figure S-2).

156

157 **MALDI-IMS Analyses.** Imaging MS analysis of tissue sections were performed on a MALDI  
158 TOF/TOF UltrafleXtreme mass spectrometer equipped with SmartBeam II Nd:YAG/355 nm  
159 laser operating at 1 kHz providing a laser spot diameter down to ~10µm for the 'minimum'  
160 focus setting (Bruker Daltonics).<sup>29</sup> As the laser beam energy profile (structured) and  
161 instrumental setup of the here used MALDI instrumentation do not facilitate straight forward  
162 measurement of exact laser fluence value at a flat target surface,<sup>29</sup> detailed information  
163 about the laser pulse energy settings is provided as follows: Global laser attenuator setting  
164 was kept stable at 10% throughout all the experiments and the laser focus set to minimum.  
165 Attenuator offset was 40% and attenuator range was 10%, for the minimum laser focus. The  
166 laser shot count of the instrument unit used for this experimentation was about 1501245k (in  
167 ~9 months age).

168 The effect of laser energy and number of shots on matrix cluster intensity was evaluated on  
169 blank glass slides covered with 120µg/cm<sup>2</sup> sublimated matrix. Varying laser pulse energies  
170 (5% increments over attenuator range: 0 to 100%) with n=10 shots were investigated and  
171 number of laser shots (5, 20, 50, 100, 300, 500) were evaluated at threshold laser energy  
172 (global offset 10% and attenuator offset 40% with the attenuator/density wheel set to 0%).  
173 Here the signal intensity (SI) of all 1,5-DAN matrix derived cluster peaks was determined  
174 using peak picking (centroid, S/N 3) in flexAnalysis (v 3.0, Bruker Daltonics). The mean  
175 values were statistically compared using ANOVA and Tukey posthoc analysis in origin (v8.1  
176 originlab, Northampton, MA).

177 MS data acquisitions were performed in reflective ion mode over a mass range of 300-2000  
178 Da with a source accelerating voltage of 25kV in positive and 20kV in negative polarities. The  
179 detector gain value was kept stable at 2626 V for both ionization modes. A mass resolution  
180 of M/ΔM 20 000 was achieved in the lipid mass range (i.e., 650–1000 Da). External

181 calibration was carried out using peptide calibration standard I (Bruker Daltonics). Image data  
182 were reconstructed, root mean square (RMS) normalized and visualized using Flex Imaging  
183 v3.0 (Bruker Daltonics). Lipid classifications were determined by comparing mass accuracy  
184 data with the LIPID MAPS database (Nature Lipidomics Gateway, [www.lipidmaps.org](http://www.lipidmaps.org)).

185

186 **Immunohistochemistry/Fluorescence and H&E Staining.** Prior to staining, sections were  
187 rinsed in absolute EtOH for 60s, fixed in 95%EtOH/5%AcOH at -20°C for 9 min, 70%EtOH at  
188 -20°C for 30sec, 70%EtOH at RT for 30sec, followed by 5min PBS, and 5min PBST (0.1%  
189 v/v Tween 20) wash at RT. Tissue was blocked for 1 hour at RT with blocking solution  
190 (PBST, 5% NGS, 2% BSA), followed by overnight primary antibody incubation at 4°C. The  
191 following morning, sections were washed 3x5min with PBST and stained with fluorescent  
192 secondary antibodies for 1h at RT. Finally, tissues were washed 3x5min with PBST, and  
193 mounted with Prolong Gold Antifade Mountant with 4',6-diamidino-2-phenylindole (DAPI,  
194 Thermo Fisher Scientific, Waltham, MA). Both primary and secondary antibodies were  
195 diluted in PBST containing 0.05% NGS, 0.02% BSA. Anti- $\beta$ III-tubulin (1:250, Abcam,  
196 Cambridge, UK) and Anti-Glial Fibrillary Acidic Protein (GFAP, 1:500, Abcam,) primary  
197 antibodies were used. Goat anti-rabbit IgG conjugated to Alexa Fluor 488 (Thermo Fisher  
198 Scientific) and goat anti-mouse IgG conjugated to Alexa Fluor 555 (Thermo Fisher Scientific)  
199 were used for visualization. Sections stained in diluent solution without primary antibodies,  
200 served as negative control. Imaging was performed using a wide field microscope (Axio  
201 Observer Z1, Zeiss, Jena, Germany) using 10x air objective for overview images and 100x  
202 oil objective for investigation of laser ablation effects. Image processing was done using the  
203 ImageJ software (<http://rsb.info.nih.gov/ij/>). For H&E staining, after MSI the matrix was  
204 washed away using 2x1 minute submersions in 100% EtOH. Tissue was rehydrated in 70%  
205 EtOH, 50% EtOH and milliQ water, 2 minutes each. The slide was placed in hematoxylin  
206 (HistoLab Products, Västra Frölunda, Sweden) for 2 minutes and washed with water for 2  
207 minutes. The slide was then counterstained in 0.2% Eosin (HistoLab Products) for 2 minutes  
208 and washed in water for 2 minutes. The section was finally washed and dehydrated in



209 50%EtOH, 70% EtOH and 100% EtOH for 1 minute each. Tissue was mounted with  
210 Permout mounting medium (eBioscience, Thermo Fisher Scientific). For fluorescent amyloid  
211 staining, after MALDI-IMS analysis, sections were rinsed in absolute EtOH for 60s, fixed in  
212 absolute EtOH at -20 °C for 8 min, 70%EtOH at -20 °C for 30 s, 70%EtOH at RT for 30 s,  
213 and rinsed for 5min in PBS both prior and after staining. For amyloid staining, 30 min  
214 incubation in heptameric formyl-thiophene acetic acid (h-FTAA), diluted to a final  
215 concentration of 3 mM in PBS, was used. Prior to imaging, the tissue was mounted with  
216 Prolong Gold antifade reagent (Thermo Fisher Scientific) and dried for 2 h at RT. Imaging  
217 was performed using a wide field microscope (Zeiss Axio Observer Z1).

218

## 219 **RESULTS AND DISCUSSION**

220 In the present study, we investigated the suitability of high spatial resolution lipid imaging  
221 using MALDI IMS for subsequent immunofluorescent staining. To overcome lateral analyte  
222 diffusion issues as commonly observed with wet matrix coating approaches (e.g. nebulizers  
223 and airbrushes), we investigated sublimation based approach for matrix deposition and lipid  
224 imaging prior to subsequent immunohistochemistry and fluorescent staining. Histology-  
225 compatibility of laser ablation process has been studied in detail.

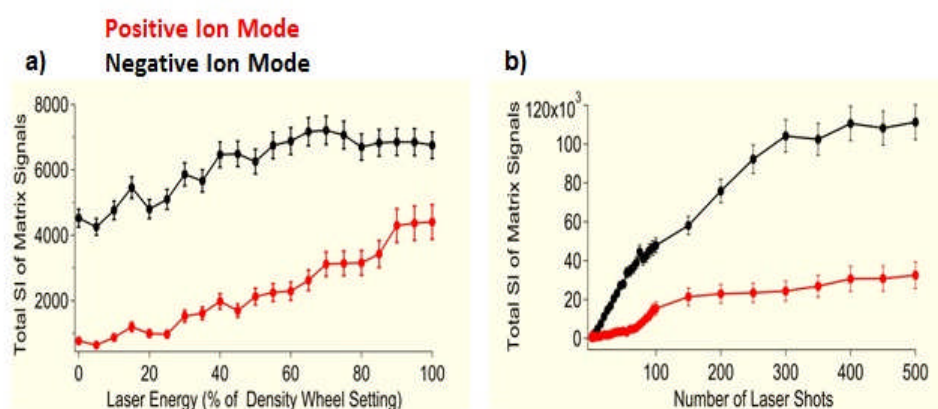
226

### 227 **Reducing Matrix Cluster Formation Induced by Laser Irradiation.**

228 Interaction of laser energy with matrix compounds is the crucial step for enhanced ion yields  
229 in MALDI-MS analysis since all matrix compounds have different optical and physico  
230 chemical properties.<sup>32</sup> In the present study, commonly used matrix compounds, including  
231 DHB, HCCA and 1,5-DAN were investigated for sublimation and neuronal lipid imaging in  
232 rodent brain in both ionization modes. The sublimation protocol was used with optimized  
233 amounts of deposited matrix in accordance with previously described results.<sup>31</sup> Here,  
234 sublimation of DHB and HCCA gave poorer lipid spectral quality (600-1000Da) with the

235 same laser fluences as compared to 1,5-DAN sublimation and MALDI IMS, particularly in  
236 negative ion mode (Supporting Information Figure S-3). In UV-MALDI, increased laser  
237 fluences result in high-intensity matrix signals beside fragmentation of matrix- and analyte  
238 molecules, which causes deterioration of the spectral quality and matrix suppression  
239 effect.<sup>32, 33</sup> Indeed, even slightly increased laser fluences resulted in matrix cluster formation  
240 when using sublimation of 1,5-DAN for MALDI IMS (Figure 1).

241 Upon laser irradiation, 1,5-DAN shows a unique behavior with respect to radical formation in  
242 contrast to other matrix compounds. Odd-electron radical ion species are  $M-H^+$  readily  
243 formed rather than  $M-H^+$  ions, which is justified by its low ionization energy.<sup>31</sup> We  
244 investigated the effect of laser pulse energy and number of laser shots on the total signal  
245 intensity of matrix derived signals from sublimation based matrix deposition. Increasing laser  
246 pulse energy and number of laser shots resulted in a sharp increase in the total signal  
247 intensity of all matrix derived signals in both positive and negative polarities (Figure 1).



248  
249 **Figure 1.** Effect of a) laser pulse energy (10 laser shots) and b) number of laser shots (at threshold  
250 laser pulse energy) on the total signal ion intensity of matrix derived peaks from a sublimation based  
251 matrix coating ( $120\mu\text{g}/\text{cm}^2$ ). Data collected both in positive (red) and negative (black) ionization  
252 modes. Error bars: SD, (n=3). For both ion modes, statistical significance ( $p < 0.05$ ) was  
253 observed e.g. between 0 and 15% and 0 and 30% in a) as well as for 0 and 100 shots in b).

254

255 Formation of matrix cluster ions was more prominent in negative ionization mode at the  
256 same levels of laser fluences as compared with positive ionization mode (Figure1). This  
257 could be explained by distinct reductive properties and radical ion transfer abilities of 1,5-  
258 DAN compared with other matrices.<sup>31, 34</sup> Here, negative radical species produced by laser  
259 irradiation ( $M^{\cdot-}$ ) were shown to cause further reduction reactions via producing  $H^{\cdot}$  radicals.<sup>31</sup>  
260 This can in turn give rise to a larger number and more intense peaks of negatively charged  
261 matrix cluster ions as compared with positively charged cluster ion species. Therefore, using  
262 1,5-DAN as a MALDI matrix could facilitate efficient gas phase ionization of lipid species with  
263 readily ionized 1,5-DAN matrix ions with very low-energy laser irradiation, particularly in  
264 negative ionization mode.

265

266 **Histology Compatibility and Spectral Quality of MALDI-IMS.** Beyond extensive matrix  
267 cluster ion formation and diminished sensitivity by oversampling<sup>35</sup>, high laser pulse energies  
268 and large number of laser shots have a severe impact on tissue integrity and morphology.  
269 This in turn may result in poor histological information after MALDI-IMS analysis. Again, the  
270 choice of matrix is very relevant as it can have a substantial effect with respect to tissue  
271 distortion during desorption-ionization process due to the distinct molar UV absorptivity  
272 values and other physicochemical properties of the different UV absorbing matrix  
273 compounds.<sup>32</sup> For the here investigated matrices, DHB, HCCA and 1,5-DAN, DHB and  
274 HCCA gave inferior lipid signal intensities (Supporting Information Figure S-3), which in turn  
275 would require higher laser energies for DHB and HCCA in order to obtain a comparable IMS  
276 spectral quality. This further supports the hypothesis that 1,5-DAN based MALDI is  
277 characterized by more gentle desorption and ionization process as compared to other  
278 matrices. Moreover, the reduced laser energy and number of shots used for 1,5-DAN might  
279 result in reduced tissue distortion as compared to DHB and HCCA, where higher laser  
280 energies are needed.

281 In order, to investigate the histology-compatibility of MALDI-IMS analysis, four different  
282 regions within a mouse brain cerebellum, including the molecular and granular layers of the  
283 cerebral cortex and the cerebral white matter (Figure 2a). The regions were analyzed with  
284 different MALDI parameters in negative polarity using 1,5-DAN sublimation. This included  
285 varying laser pulse energies and number of laser shots (Figure 2b,c). The impact on tissue  
286 morphology was then evaluated by means of subsequent IHC and fluorescent staining  
287 experiments (Figure 2a).

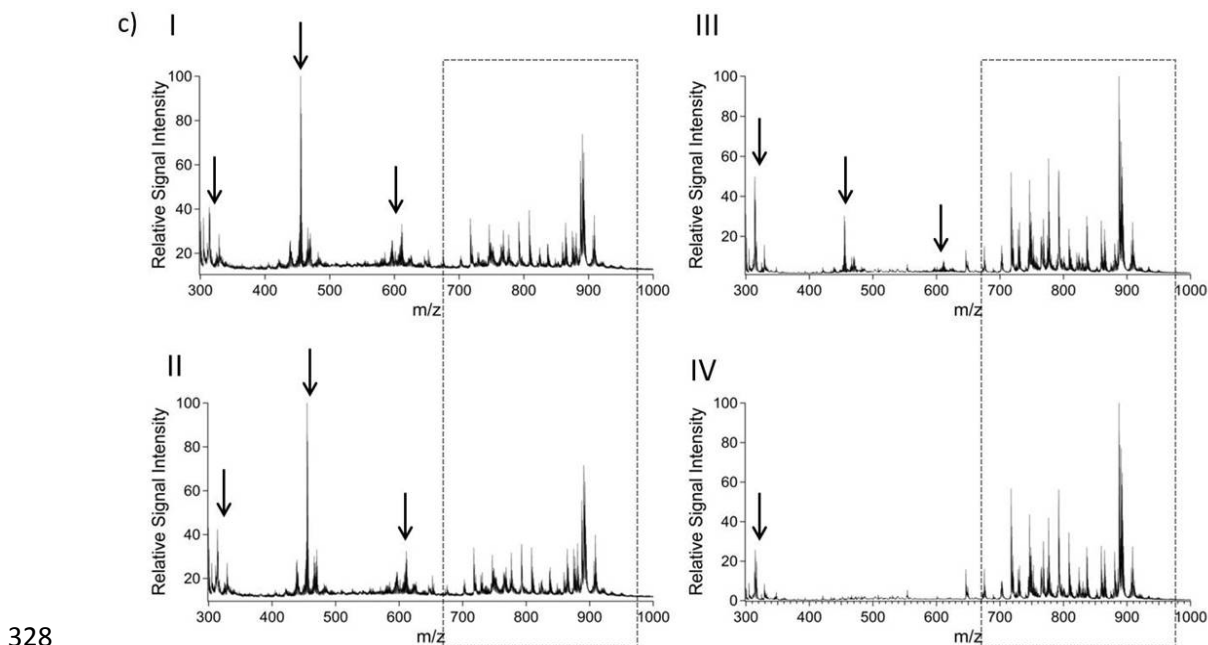
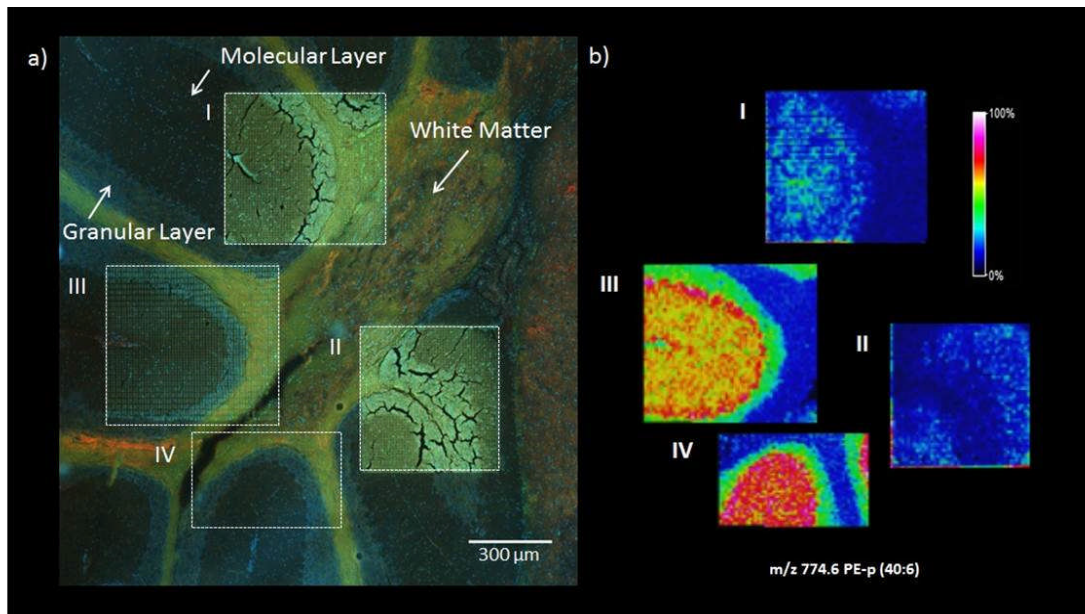
288 Here, we observed that high laser pulse energies (50% density wheel) resulted in tissue  
289 distortion with 5 and 100 laser shots (Figure 2a I-II). Moreover, this was accompanied with  
290 poor MALDI-IMS image quality (Figure 2b I-II) as well as higher number and intensity of 1,5-  
291 DAN cluster ions in between 300-650 Da mass range (Figure 2c I,II). These extensive  
292 clusters resulted furthermore in suppressed lipid signals (Figure 2c I,II). In contrast, MALDI  
293 experiments with low laser pulse energy (threshold energy level), were efficient to protect  
294 tissue integrity (Figure 2a III-IV) and improved MALDI imaging data. However, a higher  
295 number of low-energy laser shots (100) still resulted in image distortion, showing signs of  
296 laser ablation in the IHC images (Figure 2a III) and intense matrix clusters between 300-650  
297 Da (Figure 2c III).

298 On the other hand, cerebral white matter was found to be more resistant to higher laser  
299 pulse energies and higher number of laser shots, showing less signs of damage compared  
300 to molecular and granular layers (Figure 2a I-II). This fact points out the great importance of  
301 mechanical properties of biological tissues to laser ablation, as both the elasticity and  
302 strength of the tissues can modulate the kinetics and dynamics of the ablation process.<sup>25</sup>  
303 The resistant of white matter to the energetic laser pulses and local heating by nanosecond  
304 pulse durations can be explained by the superior rigidity as this region consists mainly of  
305 myelinated fiber tracts.<sup>36</sup> In turn, the higher susceptibility to laser ablation effects for the

306 molecular- and granular layer can be explained by their soft tissue properties as these layers  
307 consist mainly of cell bodies<sup>25</sup> with less myelin content.<sup>36</sup>

308 Laser ablation effects on tissue morphology were further investigated on different areas of  
309 molecular layer within the cerebellum in a sagittal mouse brain tissue section. By varying  
310 the number of laser shots (5, 20, 50, 100, 200, 300, 500) using threshold laser energy,  
311 tissue and fluorescent signal distortions were observed starting with 50 laser shots and  
312 getting prominent with  $\geq 100$  laser shots (Supporting Information Figure S-4I-II). Moreover,  
313 epitope degradation was prominent as indicated by the decreased tubulin and GFAP  
314 immunofluorescence, while the DAPI signal was less affected (Supporting Information  
315 Figure S-4II). In addition, control experiments were performed to investigate whether the  
316 increased fluorescence background on the laser ablation sites is a result of sole tissue  
317 damage and autofluorescence or non-specific binding of primary and secondary antibodies  
318 on the ablated raster sites. Therefore, control experiments were performed without using any  
319 or solely a secondary antibody following MALDI-IMS analysis with varying number of laser  
320 shots. The results indicate that ablation-damaged tissue areas display increased  
321 background in both blue and green channels in fluorescence microscope images  
322 (Supporting Information Figure S-5II), while no significantly higher fluorescent signal was  
323 observed with staining using the fluorescently labelled secondary antibody (Supporting  
324 Information Figure S-5I). This suggests a dominant effect of tissue distortion and  
325 consequently autofluorescence rather than unspecific binding (Supporting Information Figure  
326 S-5).

327



328

329 **Figure 2.** Subsequent IHC and fluorescent staining images of four different sections on mice  
 330 cerebellum region analyzed with different parameters of MALDI imaging mass spectrometry. a I) 100  
 331 of 50%-energy laser shots a II) 5 of 50%-energy laser shots a III) 100 of threshold-energy laser shots  
 332 and a IV) 5 of threshold-energy laser shots in reflective negative ion mode followed by  
 333 immunohistochemistry and fluorescent staining. Corresponding single ion images of PE-p (40:6, m/z  
 334 774.6) and full range MS spectra of the same sections were shown in b I-IV and c I-IV, respectively.  
 335 Highlighted regions in the spectra (650-950 Da) show relative signal intensity of lipids. Arrows in  
 336 between 300-650 Da mass range indicate 1,5-DAN matrix cluster ions. %-energy stands for density  
 337 wheel setting. Imaging data were acquired with a spatial resolution of 10 $\mu$ m. Anti-gial fibrillary acidic  
 338 protein (GFAP, green), anti- $\beta$ III-tubulin (red) and fluorescent stain 4,6-diamidino-2-phenylindole (DAPI,  
 339 blue) were used to visualize radial glial cells, cytoskeleton and cell nuclei, respectively; allowing to  
 340 highlight the molecular layer, the granular layer and the white matter.

341

342 Interestingly, using solely threshold laser energy (i.e. global offset: 10%, attenuator offset:

343 40%, 0% density wheel), with only 5 laser shots, proved to maintain histological morphology

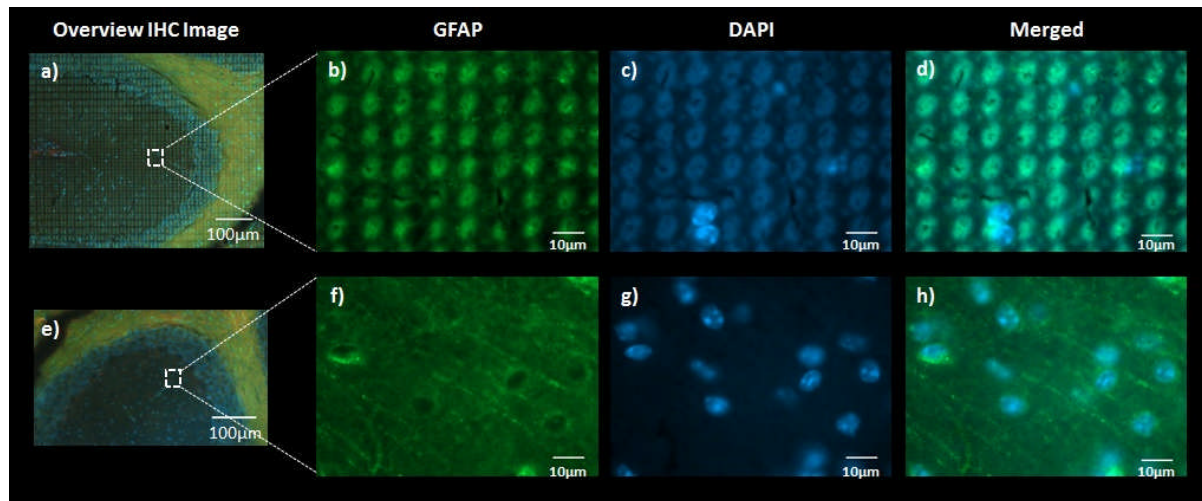
344 with an undistorted image quality and fluorophore signal as well as protection of protein  
345 epitopes (Figure 2a IV). These parameters resulted in enhanced spectral information and  
346 IMS data quality (Figure 2b IV), which is further highlighted by the single ion images of  
347 phosphatidylethanolamine (PE-p 36:4) indicating a substantial signal increase of this species  
348 in the molecular layer (Figure 2b IV). Moreover, this approach resulted in a general  
349 enhancement of lipid signals (in 650-950 Da mass range), as compared to collection of 100  
350 laser shots, along with suppression of matrix clusters between 350-650 Da (Figure 2c IV).

351 These results can be explained by the comparable low ionization energy of 1,5-DAN.  
352 Although understanding of desorption/ionization process is still unachieved due to the  
353 complex ionization processes in desorbed matrix-assisted laser desorption plume<sup>28, 37</sup>,  
354 analyte ion formation in UV-MALDI was shown to be a convolution of analytes pre-charged  
355 in the solution (Lucky-Survivor Model)<sup>38</sup> as well as ionization of neutral analytes by the  
356 ionized matrix ions in the gas phase.<sup>37, 39, 40</sup> Therefore, low energies sufficient for ionization  
357 of 1,5-DAN molecules can enhance gas phase ionization of lipids by readily ionized matrix  
358 ions even at very low laser fluences, particular in negative ion mode. As a result, by  
359 minimizing the oversampling effect and to increase the ionization sensitivity<sup>35</sup>, this “gentle”  
360 irradiation does further enable improved correlation of well-preserved molecular tissue  
361 morphology with lipid signals, as illustrated for PE-p (40:6, m/z 774.6) species.

362

363 **Microscale Effects of Laser Ablation following MALDI-IMS.** Using only a low number of  
364 laser shots at low laser pulse energies allowed for comprehensive MALDI-IMS and  
365 subsequent fluorescence microscopy of the molecular layer, granular layer and the white  
366 matter of the cerebellum, as visualized with antibodies towards glial fibrillary acidic protein  
367 (GFAP) and  $\beta$ III-tubulin as well as DAPI for nuclear staining (Figure 3).

368



369

370 **Figure 3.** High resolution immunohistochemistry and fluorescent staining images following MALDI-  
 371 IMS. Immunohistochemistry and fluorescent staining were performed on two cerebellar regions of  
 372 interest (ROI-I: a-d, corresponding to Fig. 2a-III and ROI-II: e-h, corresponding to Fig. 2a-IV). High  
 373 resolution fluorescent microscopy (100x) shows no overlap of laser ablation after MALDI-IMS with (b-  
 374 d) 100 shots and (f-h) 5 shots with laser energy set to threshold (0% density wheel setting). (f-h) Low  
 375 number of laser shots at threshold energy allowed for visualization of radial glial cells (GFAP, green)  
 376 and cell nuclei (DAPI, blue) without laser ablation damage on the brain tissue as compared to b-d  
 377 where tissue distortion is observed. Magnification a,e: (10x); b-d, f-h: (100x).

378

379 In particular, by using a higher magnification (100x), a clear visualization of cellular  
 380 structures including nuclei (DAPI) and cytoplasmic protein accumulation (GFAP) was  
 381 possible as laser ablation induced interferences on the tissue surface were abolished, when  
 382 acquiring IMS data with only 5 laser shots (Figure 3 f-h) as compared to collection of 100  
 383 shots (Figure 3 b-d). The results highlight that the application of 1,5-DAN sublimation and  
 384 gentle laser irradiation for lipid MALDI-IMS in negative ion mode preserves the entire  
 385 histological information for subsequent IHC analysis and suggests thereby enhanced  
 386 correlation of molecular information with histological features.

387 On the other hand, the IHC results were compared to H&E staining following MALDI IMS.  
 388 H&E is commonly used after MALDI-IMS analysis on the same tissue section to correlate  
 389 IMS data with histological features.<sup>23</sup> It is a non-specific chemical staining method, which is  
 390 used to evaluate all histological structures and cells that take up the staining dye. As this is a  
 391 general protein staining method, i.e. not specific for any unique epitope(s), it may not reveal  
 392 distortions of protein structures and cells occurring as a consequence of laser ablation

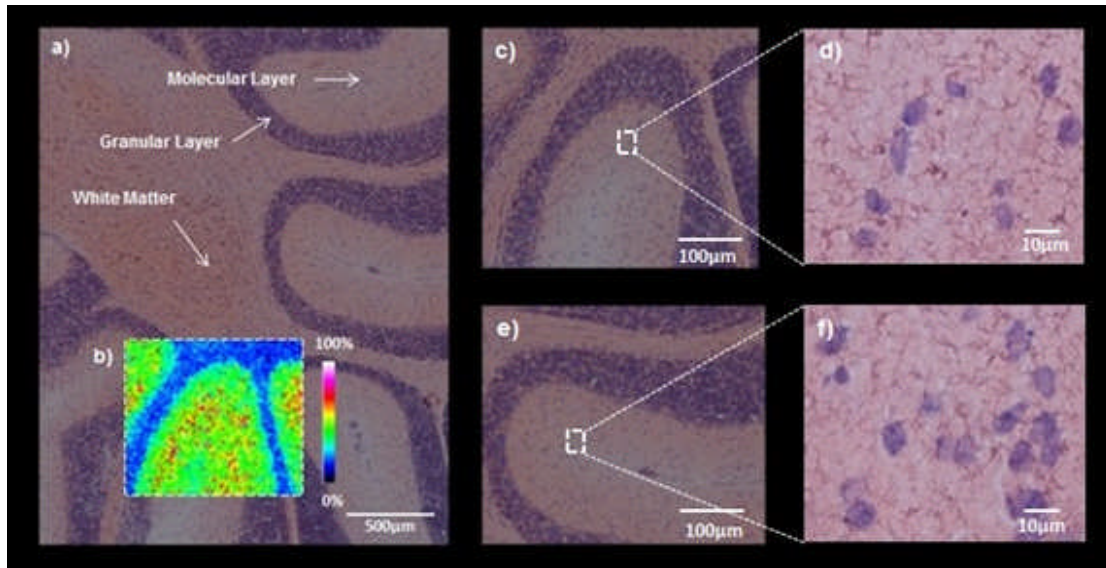


393 effects caused by irradiation with energetic laser pulses during desorption-ionization  
394 process.

395 Indeed, in contrast to IHC and fluorescent staining, high resolution microscopy images of  
396 subsequent H&E staining did not show any laser ablation effects on tissue morphology when  
397 acquiring MALDI-IMS data with 200 laser shots per pixel area at threshold laser pulse energy  
398 (Figure 4). Furthermore, control experiments have been performed using exactly the same  
399 tissue pre-treatment for both H&E and IHC staining experiments. Laser ablation effects on  
400 the tissue morphology were further investigated on different sections of molecular layer with  
401 varying number of laser shots (5, 50, 100, 200, 300, 500) using threshold laser energy. Here,  
402 high-resolution microscopy images of H&E staining indicated no signs of laser ablation  
403 effects up to 500 laser shots (Supporting Information Figure S-6).

404 These results can be explained by the non-specific staining of H&E in which hematoxylin and  
405 eosin stain general nucleic acids and proteins <sup>41</sup>. H&E staining involves application of  
406 hemalum that stains nuclei of cells (and a few other objects, such as keratohyalin granules  
407 and calcified material).The nuclear staining is followed by counterstaining with an aqueous or  
408 alcoholic solution of eosin Y, which stains eosinophilic structures in various shades of red,  
409 pink and orange.<sup>41</sup> Interestingly, in the fluorescent staining experiments, the DAPI staining  
410 intensity was largely unaffected as compared to the antibody labelling (Figure 3c and  
411 Supporting Figure S4). This further supports the theory that epitope availability is more  
412 sensitive to laser ablation effects than unspecific histological staining as observed for DAPI  
413 and H&E.

414



415

416 **Figure 4.** High resolution H&E staining after MALDI-IMS analysis on the same tissue section. a) H&E  
 417 stained cerebellar region. b) Single ion image of PE-p 40:6 ( $m/z$  774.6) from cerebellar region  
 418 analyzed with MALDI-IMS by acquiring 200 laser shots (at threshold laser pulse energy) per pixel with  
 419  $10\mu\text{m}$  spatial resolution. High resolution microscopy images of (c,d ) MALDI-IMS analyzed and e, f)  
 420 non-analyzed regional microscopy images show no laser ablation effects with c,e) 20x and d,f) 100x  
 421 magnification.

422

423 This in turn is of great relevance, as MALDI imaging applications are commonly based on  
 424 subsequent H&E staining in order to validate and correlate the ion signals to  
 425 histopathologically relevant features. As H&E staining is unspecific, consequences of tissue  
 426 distortion and ion delocalization cannot be detected and quantified. This can in turn lead to  
 427 misalignment issues and false positive results for correlation of multimodal imaging data and  
 428 biological interpretation (Figure 4c,d).

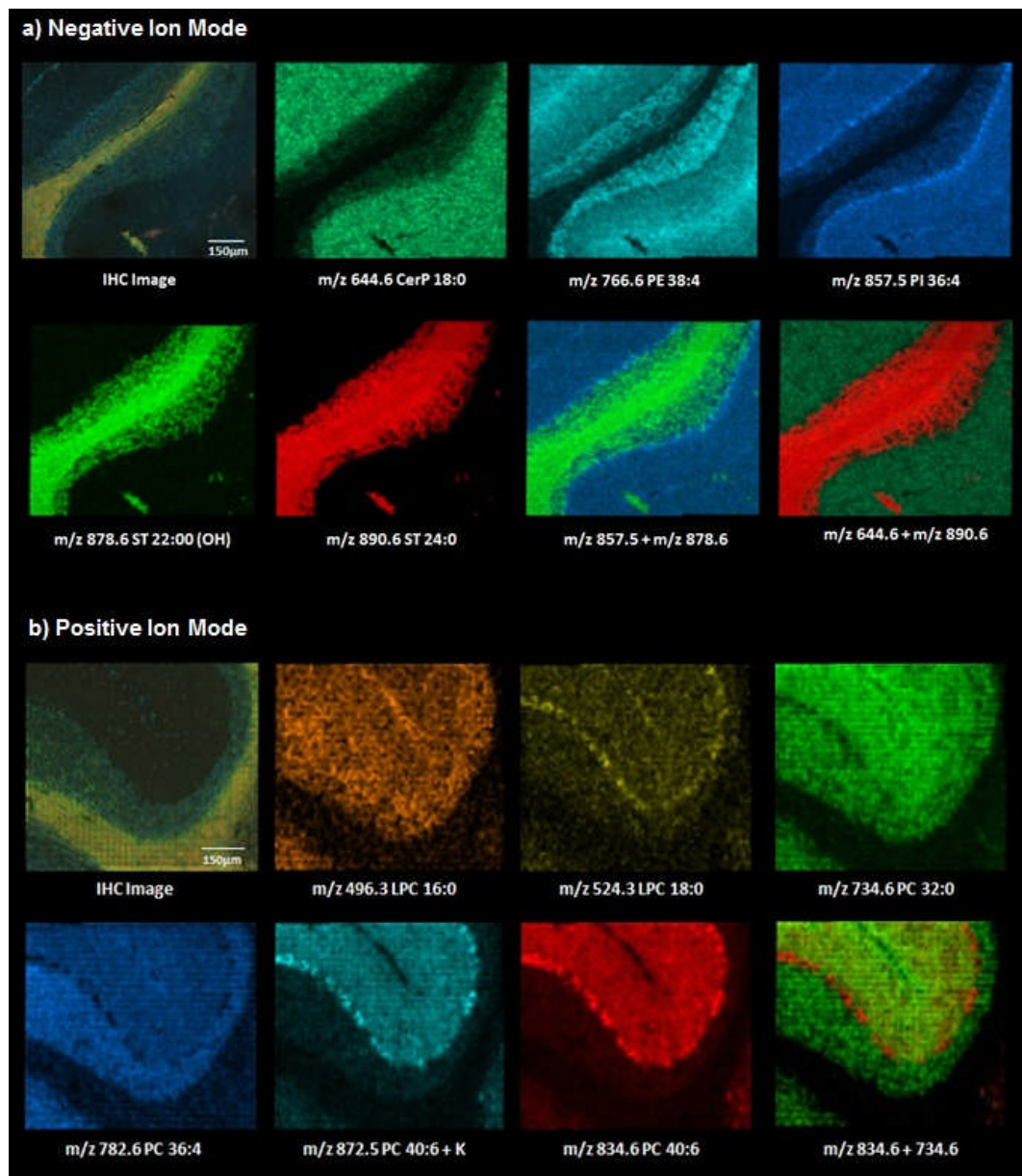
429

430 **High Resolution MALDI IMS with Subsequent Immunofluorescent Staining.** High-

431 resolution MALDI-IMS is a suitable approach for improved correlation of MS ion image data  
 432 with histological features.<sup>11, 42</sup> We achieved a spatial resolution of  $10\mu\text{m}$  in both positive and  
 433 negative ionization modes to reach spatially detailed information to be correlated with  
 434 histological features which were visualized by subsequent IHC and fluorescent staining  
 435 (Figure 5a, b). In this case, when using minimum laser focus parameter, no laser ablation  
 436 overlap was observed with 100 of low-energy laser shots (Figure 3a-d) and even no signs of

437 laser ablation with low-energy few number of laser shots (Figure 3e-h) in negative ionization  
438 mode. Using 1,5-DAN sublimation in conjunction with gentle irradiation in MALDI-IMS  
439 analysis of neuronal lipids allowed for subsequent immunohistochemistry analysis with  
440 minimized loss of histological information in negative ion mode (Figure 5a). However, the  
441 number of laser shots (n=50) at the threshold laser energy (global offset: 10%, att. offset  
442 40%, 0% density wheel) that was needed to obtain intense lipid signals was higher in positive  
443 ion mode. This can be due to the fact that 1,5-DAN as a basic matrix compound can act as a  
444 “proton sponge” during desorption-ionization process and suppress the formation of  
445 positively charged lipid ions in the gas phase. Therefore, in positive ion mode, slight signs of  
446 laser ablation effects were observed on the tissue surface after high resolution MALDI-IMS  
447 analysis. (Figure 5b)

448



449

450 **Figure 5.** High spatial resolution MALDI-IMS of lipids in both a) negative and b) positive ionization  
 451 modes from a sagittal mice cerebellum regions coated with 1,5-DAN sublimation approach and  
 452 acquired with a lateral resolution of 10µm. Anti-gial fibrillary acidic protein (GFAP, green), anti-βIII-  
 453 tubulin (red) and 4,6-diamidino-2-phenylindole (DAPI, blue) fluorescent stain were used to visualize  
 454 radial glial cells, cytoskeleton and cell nuclei, respectively; allowing to highlight the molecular layer, the  
 455 granular layer and the white matter.

456

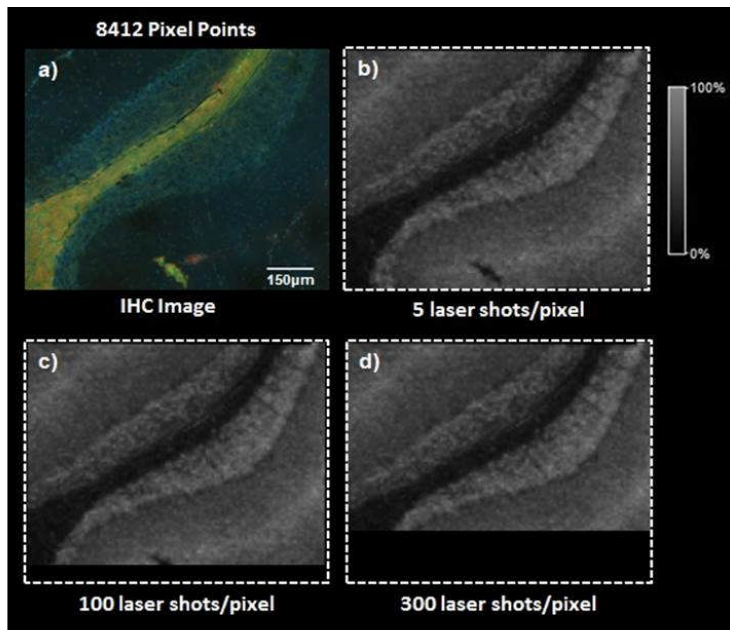
457 Here histological features of the of the cerebellar regions as outlined by fluorescence  
 458 immunostaining can be visualized and correlated with ion signals of distinct neuronal lipid  
 459 species, including ceramides (CerP 18:0, m/z 644.6), sulfatides (ST 20:4, m/z 890.6) and  
 460 phosphoethanolamines (PE 38:4, m/z 766.6) and phosphoinositols (PI 36:4, m/z 857.5) in  
 461 negative ion mode (Figure 5a) and phosphatidylcholines (PC 32:0, m/z 734.6) and

462 lysophosphatidcholines (LPC 16:0, m/z 496.3 and LPC 18:0, m/z 524.3) in positive ion  
463 mode (Figure 5b). In detail, PE 38:4 and PC 36:4 were found to localize to the cell body  
464 dense granular layer as visualized with DAPI, highlighting their role in mammalian neuronal  
465 cell membranes. In addition, together with CerP 18:0 and PC 40:6, these species also  
466 localized to the radial glial cell rich molecular layer, as visualized with GFAP, also known for  
467 presence of granule cell derived parallel fibers. In contrast, sulfatides ST 24:0 and ST  
468 22:0(OH) predominantly localized to the white matter and in part to the granular layer. This  
469 can be tied to the abundance of long myelinated axons in the white matter (as visualized with  
470 anti- $\beta$ III-tubulin) and presence of oligodendrocytes in the granular layer where sulfatides are  
471 one of the main lipid constituents.<sup>43</sup>

472

473 **Enhanced Speed of Data Acquisition for High Spatial Resolution in Negative Ionization**  
474 **Mode.** High-speed in IMS is needed in order to obtain high spatial resolution ion images of  
475 larger tissue areas in a reasonable acquisition time<sup>35</sup>, particularly for sublimated tissue  
476 samples, where volatile matrices are used that are subjected to high vacuum in the ion  
477 source.<sup>44</sup> For example, acquisition of a small cerebellar region requires 8412 pixel points to  
478 be analyzed with 10 $\mu$ m spatial resolution (Figure 6a). For high-speed MALDI-TOF IMS, there  
479 have been technological advances including high repetition rate lasers, continuous raster  
480 sampling, and synchronized high repetition laser beam with rapidly moving sample stage.<sup>35</sup>  
481 <sup>44, 45</sup> However, the number of laser pulses required per pixel point to obtain intense lipid  
482 signals can have a substantial effect on the speed of data acquisition.

483



e)

Number of laser shots per pixel	Acquisition time (min)	Acquisition speed (sec/pixel)	Percent area (8412 pixel points) imaged in 142 minutes
5	142	1.0128	100%
50	148	1.0554	96%
100	155	1.1052	92%
200	169	1.2054	84%
300	183	1.3050	78%
400	197	1.4051	72%
500	211	1.5048	67%

484

485 **Figure 6.** Illustration of MALDI-IMS experiment of lipids in negative ionization mode using 1,5-DAN  
 486 sublimation, given with a defined a) IHC image of cerebellar region (8412 pixel points with 10µm  
 487 spatial resolution) and represented by ion image of PE 38:4, m/z 766.6 b)-d). The areas indicate the  
 488 approximate proportion of the cerebellar region that can be measured with indicated number of laser  
 489 shots b) 5, c) 100, d) 300 per pixel point. e) comparative speed of acquisition and percent area of a  
 490 cerebellar region (8412 pixel points) that can be imaged using different number of laser shots per pixel  
 491 area at 10µm spatial resolution.

492

493 Using the optimized 1,5-DAN sublimation approach, only 5 laser shots were needed for  
 494 negative ion lipid imaging, reducing the required amount of time to generate a pixel spectra  
 495 substantially (Figure 6b,e). Considering the number of pixel points (several tens of  
 496 thousands) needed to image a whole brain tissue section at high spatial resolutions, along  
 497 with the required technical- and biological replicates, this approach can substantially reduce

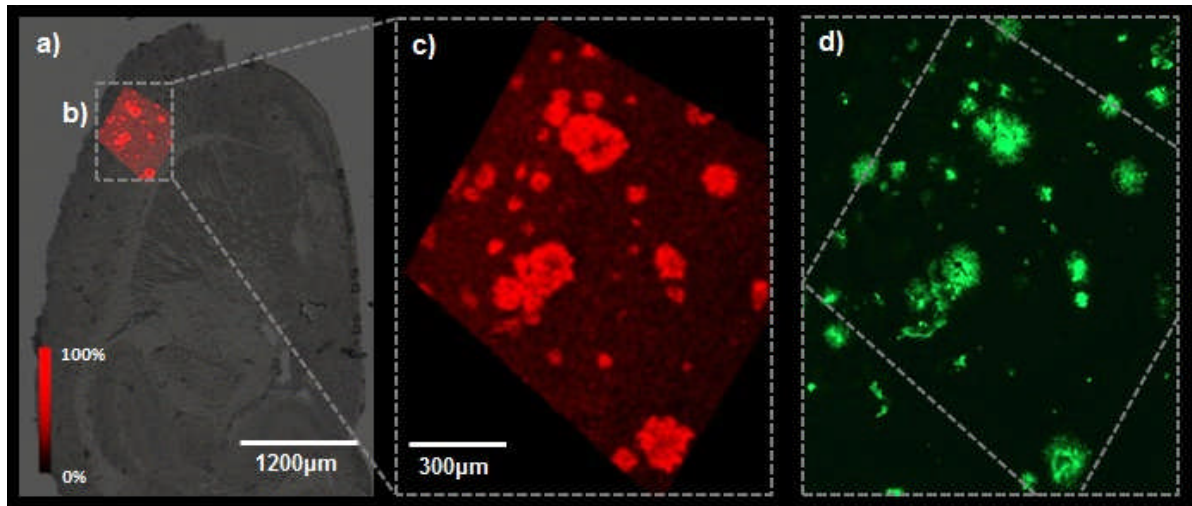
498 the necessary acquisition time to a more reasonable level for biological and clinical  
499 applications.

500

501 **Amyloid- $\beta$  Plaque Associated Neuronal Lipids Imaging Using High Spatial Resolution**  
502 **MALDI-IMS with Subsequent Fluorescent Staining.** Finally, in order to further demonstrate  
503 the potential and relevance of the here described method, we performed high resolution IMS  
504 and subsequent fluorescent staining on brain tissue in transgenic Alzheimer's disease (AD)  
505 tgSwe mice. AD is a chronic, neurodegenerative disorder which is characterized by the  
506 formation of protein deposits in the brain including intercellular neurofibrillary tangles  
507 consisting of hyperphosphorylated tau protein<sup>46</sup> and extracellular amyloid- $\beta$  plaques<sup>47</sup>.  
508 Recent studies suggest that dysregulated neuronal lipid metabolism may be linked to AD  
509 pathogenesis, potentially by influencing amyloidogenic processing of the transmembrane  
510 amyloid precursor protein (APP) and/or the aggregation of amyloid  $\beta$  (A $\beta$ ).<sup>48, 49</sup> Therefore,  
511 multimodal chemical imaging tools are needed in order to delineate A $\beta$  plaque-associated  
512 neuronal lipid species. We therefore investigated TgSwe mice that overexpress  $\beta$ -amyloid  
513 (A $\beta$ ) due to having the human *APP* KM670/671NL mutation and develop intraneuronal A $\beta$   
514 aggregates at six months and extracellular plaques at 12 months. We utilized the here  
515 described method for rapid, high-spatial resolution (10 $\mu$ m), histology-compatible MALDI-IMS  
516 of neuronal lipid species on a cortical region followed by subsequent fluorescent amyloid  
517 staining<sup>50</sup> of cortical A $\beta$  aggregates (Figure 7).

518

519



520

521 **Figure 7.** Imaging of amyloid plaque associated neuronal lipid species using high resolution MALDI-  
 522 IMS with subsequent fluorescent staining. a) bright-field image of sagittal tgSwe mice brain tissue  
 523 section. b) high resolution (10 $\mu$ m) MALDI-IMS analyzed cortical region using the method in Fig 2a IV.  
 524 c,e) ion image of Ceramide (18:0, m/z 564.6) species which is correlated with d,f) high resolution  
 525 fluorescent microscopy image of amyloid aggregates.

526

527 The results demonstrate a conclusive correlation of MALDI-IMS derived ion image data of  
 528 e.g. ceramide species (18:0, m/z 564.6) and fluorescent microscopy images of amyloid  
 529 aggregates. This in turn suggests a role of plaque-associated ceramide elevation in AD  
 530 pathology as previously reported in AD patients<sup>51</sup> as well as in another transgenic AD models  
 531 <sup>14</sup>. Identification of ceramide (18:0, m/z 564.6) species was based on its characteristic  
 532 fragment ions<sup>52</sup> using MALDI-LIFT™ based MS/MS that was performed directly on the  
 533 plaques in situ (Supporting Information, Figure S-7). Here, an accurate correlation of the IMS  
 534 data to IHC annotated amyloid plaques is essential in order to correctly identify plaque  
 535 pathology associated lipid species. This highlights further the relevance of non-impaired  
 536 tissue and protein morphology as achieved with the here presented multimodal imaging  
 537 methodology.

## 538 CONCLUSIONS

539 In this study, we demonstrated that elaborate optimization of MALDI-IMS parameters  
 540 enhanced the performance of the MALDI imaging of brain lipids. By using a comparably low-  
 541 ionization energy matrix compound, 1,5-DAN, histological information after IMS analysis was



542 preserved along with enhanced lipid spectra quality and data acquisition speed. Subsequent  
543 immunofluorescent stainings revealed laser fluence-dependent distortion of tissue  
544 morphology, which was not detected with commonly used H&E staining. Finally, the  
545 improved methodology was successfully applied to spatially profile amyloid plaque-  
546 associated neuronal lipid species such as ceramide (Cer18:0, m/z 564.6) in a transgenic  
547 mouse model of Alzheimer's disease. The technique can be a powerful approach to probe  
548 lipid pathology of neurodegenerative diseases enhancing the corresponding information of  
549 MALDI-IMS and immunohistochemistry and/or fluorescent staining methods.

550

## 551 REFERENCES

- 552 [1] van Meer, G. (2005) Cellular lipidomics, *The EMBO journal* 24, 3159-3165.  
553 [2] Shevchenko, A., and Simons, K. (2010) Lipidomics: coming to grips with lipid diversity,  
554 *Nature reviews Molecular cell biology* 11, 593-598.  
555 [3] Dowhan, W. (1997) Molecular basis for membrane phospholipid diversity: why are there  
556 so many lipids?, *Annual review of biochemistry* 66, 199-232.  
557 [4] Di Paolo, G., and Kim, T.-W. (2011) Linking lipids to Alzheimer's disease: cholesterol and  
558 beyond, *Nature Reviews Neuroscience* 12, 284-296.  
559 [5] Ruipérez, V., Darios, F., and Davletov, B. (2010) Alpha-synuclein, lipids and Parkinson's  
560 disease, *Progress in lipid research* 49, 420-428.  
561 [6] Schmitt, F., Hussain, G., Dupuis, L., Loeffler, J. P., and Henriques, A. (2014) A plural role  
562 for lipids in motor neuron diseases: energy, signaling and structure, *Frontiers in*  
563 *cellular neuroscience* 8, 25.  
564 [7] Swank, R. L., and Grimsgaard, A. (1988) Multiple sclerosis: the lipid relationship, *The*  
565 *American journal of clinical nutrition* 48, 1387-1393.  
566 [8] Maxfield, F. R., and Tabas, I. (2005) Role of cholesterol and lipid organization in disease,  
567 *Nature* 438, 612-621.  
568 [9] Caprioli, R. M., Farmer, T. B., and Gile, J. (1997) Molecular Imaging of Biological  
569 Samples: Localization of Peptides and Proteins Using MALDI-TOF MS, *Analytical*  
570 *Chemistry* 69, 4751-4760.  
571 [10] McDonnell, L. A., and Heeren, R. (2007) Imaging mass spectrometry, *Mass*  
572 *spectrometry reviews* 26, 606-643.  
573 [11] Chaurand, P., Cornett, D. S., Angel, P. M., and Caprioli, R. M. (2011) From whole-body  
574 sections down to cellular level, multiscale imaging of phospholipids by MALDI mass  
575 spectrometry, *Molecular & Cellular Proteomics* 10, O110. 004259.  
576 [12] Hanrieder, J., Malmberg, P., Lindberg, O. R., Fletcher, J. S., and Ewing, A. G. (2013)  
577 Time-of-flight secondary ion mass spectrometry based molecular histology of human  
578 spinal cord tissue and motor neurons, *Analytical Chemistry* 85, 8741-8748.  
579 [13] Hanrieder, J., Phan, N. T. N., Kurczyk, M. E., and Ewing, A. G. (2013) Imaging Mass  
580 Spectrometry in Neuroscience, *ACS Chemical Neuroscience* 4, 666-679.  
581 [14] Kaya, I., Brinet, D., Michno, W., Syvanen, S., Sehlin, D., Zetterberg, H., Blennow, K.,  
582 and Hanrieder, J. (2016) Delineating Amyloid Plaque Associated Neuronal  
583 Sphingolipids In Transgenic Alzheimer's Disease Mice (tgArcSwe) Using MALDI  
584 Imaging Mass Spectrometry, *ACS Chemical Neuroscience* 8, 347-355.

- 585 [15] Hanrieder, J., Gerber, L., Persson Sandelius, Å., Brittebo, E. B., Ewing, A. G., and  
586 Karlsson, O. (2014) High resolution metabolite imaging in the hippocampus following  
587 neonatal exposure to the environmental toxin BMAA using ToF-SIMS, *ACS chemical*  
588 *neuroscience* 5, 568-575.
- 589 [16] Hanrieder, J., Ljungdahl, A., Fälth, M., Mammo, S. E., Bergquist, J., and Andersson, M.  
590 (2011) L-DOPA-induced dyskinesia is associated with regional increase of striatal  
591 dynorphin peptides as elucidated by imaging mass spectrometry, *Molecular & Cellular*  
592 *Proteomics* 10, M111. 009308.
- 593 [17] Carlred, L., Michno, W., Kaya, I., Sjövall, P., Syvänen, S., and Hanrieder, J. (2016)  
594 Probing Amyloid- $\beta$  Pathology in transgenic Alzheimer's disease (tgArcSwe) mice  
595 using MALDI Imaging Mass Spectrometry, *Journal of Neurochemistry*.
- 596 [18] Yang, J., and Caprioli, R. M. (2011) Matrix sublimation/recrystallization for imaging  
597 proteins by mass spectrometry at high spatial resolution, *Analytical chemistry* 83,  
598 5728-5734.
- 599 [19] Karas, M., and Hillenkamp, F. (1988) Laser desorption ionization of proteins with  
600 molecular masses exceeding 10,000 daltons, *Analytical chemistry* 60, 2299-2301.
- 601 [20] Thomas, A. I., Charbonneau, J. L., Fournaise, E., and Chaurand, P. (2012) Sublimation  
602 of new matrix candidates for high spatial resolution imaging mass spectrometry of  
603 lipids: enhanced information in both positive and negative polarities after 1, 5-  
604 diamionaphthalene deposition, *Analytical chemistry* 84, 2048-2054.
- 605 [21] Hankin, J. A., Barkley, R. M., and Murphy, R. C. (2007) Sublimation as a method of  
606 matrix application for mass spectrometric imaging, *Journal of the American Society*  
607 *for Mass Spectrometry* 18, 1646-1652.
- 608 [22] Murphy, R. C., Hankin, J. A., Barkley, R. M., and Berry, K. A. Z. (2011) MALDI imaging  
609 of lipids after matrix sublimation/deposition, *Biochimica et Biophysica Acta (BBA)-*  
610 *Molecular and Cell Biology of Lipids* 1811, 970-975.
- 611 [23] Deutskens, F., Yang, J., and Caprioli, R. M. (2011) High spatial resolution imaging mass  
612 spectrometry and classical histology on a single tissue section, *Journal of Mass*  
613 *Spectrometry* 46, 568-571.
- 614 [24] Walch, A., Rauser, S., Deininger, S.-O., and Höfler, H. (2008) MALDI imaging mass  
615 spectrometry for direct tissue analysis: a new frontier for molecular histology,  
616 *Histochemistry and cell biology* 130, 421-434.
- 617 [25] Vogel, A., and Venugopalan, V. (2003) Mechanisms of pulsed laser ablation of biological  
618 tissues, *Chemical reviews* 103, 577-644.
- 619 [26] Russo, R. E., Mao, X., Gonzalez, J. J., Zorba, V., and Yoo, J. (2013) Laser ablation in  
620 analytical chemistry, ACS Publications.
- 621 [27] Dufresne, M., Guneysu, D., Patterson, N. H., Marcinkiewicz, M. M., Regina, A.,  
622 Demeule, M., and Chaurand, P. (2016) Multimodal detection of GM2 and GM3 lipid  
623 species in the brain of mucopolysaccharidosis type II mouse by serial imaging mass  
624 spectrometry and immunohistochemistry, *Analytical and Bioanalytical Chemistry*, 1-9.
- 625 [28] Dreisewerd, K. (2003) The desorption process in MALDI, *Chemical reviews* 103, 395-  
626 426.
- 627 [29] Optimizing, U. (2006) laser focus profiles for improved MALDI performance Holle, Armin;  
628 Haase, Andreas; Kayser, Markus; Hoehndorf, *Journal of Mass Spectrometry* 41, 705-  
629 716.
- 630 [30] Lord, A., Kalimo, H., Eckman, C., Zhang, X.-Q., Lannfelt, L., and Nilsson, L. N. (2006)  
631 The Arctic Alzheimer mutation facilitates early intraneuronal A $\beta$  aggregation and  
632 senile plaque formation in transgenic mice, *Neurobiology of aging* 27, 67-77.
- 633 [31] Molin, L., Seraglia, R., Dani, F. R., Moneti, G., and Traldi, P. (2011) The double nature of  
634 1, 5-diamionaphthalene as matrix-assisted laser desorption/ionization matrix: some  
635 experimental evidence of the protonation and reduction mechanisms, *Rapid*  
636 *Communications in Mass Spectrometry* 25, 3091-3096.
- 637 [32] Soltwisch, J., Jaskolla, T. W., Hillenkamp, F., Karas, M., and Dreisewerd, K. (2012) Ion  
638 yields in UV-MALDI mass spectrometry as a function of excitation laser wavelength

- 639 and optical and physico-chemical properties of classical and halogen-substituted  
640 MALDI matrixes, *Analytical chemistry* 84, 6567-6576.
- 641 [33] Smirnov, I., Zhu, X., Taylor, T., Huang, Y., Ross, P., Papayanopoulos, I., Martin, S., and  
642 Pappin, D. (2004) Suppression of  $\alpha$ -cyano-4-hydroxycinnamic acid matrix clusters  
643 and reduction of chemical noise in MALDI-TOF mass spectrometry, *Analytical*  
644 *chemistry* 76, 2958-2965.
- 645 [34] Demeure, K., Quinton, L., Gabelica, V., and De Pauw, E. (2007) Rational selection of the  
646 optimum MALDI matrix for top-down proteomics by in-source decay, *Analytical*  
647 *chemistry* 79, 8678-8685.
- 648 [35] Spraggins, J. M., and Caprioli, R. M. (2011) High-speed MALDI-TOF imaging mass  
649 spectrometry: rapid ion image acquisition and considerations for next generation  
650 instrumentation, *Journal of the American Society for Mass Spectrometry* 22, 1022-  
651 1031.
- 652 [36] Weickenmeier, J., de Rooij, R., Budday, S., Steinmann, P., Ovaert, T., and Kuhl, E.  
653 (2016) Brain stiffness increases with myelin content, *Acta biomaterialia* 42, 265-272.
- 654 [37] Knochenmuss, R. (2006) Ion formation mechanisms in UV-MALDI, *Analyst* 131, 966-  
655 986.
- 656 [38] Karas, M., Glückmann, M., and Schäfer, J. (2000) Ionization in matrix-assisted laser  
657 desorption/ionization: singly charged molecular ions are the lucky survivors, *Journal*  
658 *of Mass Spectrometry* 35, 1-12.
- 659 [39] Jaskolla, T. W., and Karas, M. (2011) Compelling evidence for lucky survivor and gas  
660 phase protonation: the unified MALDI analyte protonation mechanism, *Journal of the*  
661 *American Society for Mass Spectrometry* 22, 976-988.
- 662 [40] Ehring, H., Karas, M., and Hillenkamp, F. (1992) Role of photoionization and  
663 photochemistry in ionization processes of organic molecules and relevance for  
664 matrix-assisted laser desorption ionization mass spectrometry, *Organic mass*  
665 *spectrometry* 27, 472-480.
- 666 [41] Fischer, A. H., Jacobson, K. A., Rose, J., and Zeller, R. (2008) Hematoxylin and eosin  
667 staining of tissue and cell sections, *Cold Spring Harbor Protocols* 2008, pdb.  
668 prot4986.
- 669 [42] Chaurand, P., Schriver, K. E., and Caprioli, R. M. (2007) Instrument design and  
670 characterization for high resolution MALDI-MS imaging of tissue sections, *Journal of*  
671 *Mass Spectrometry* 42, 476-489.
- 672 [43] Ishizuka, I. (1997) Chemistry and functional distribution of sulfoglycolipids, *Progress in*  
673 *lipid research* 36, 245-319.
- 674 [44] Ogrinc Potočnik, N., Porta, T., Becker, M., Heeren, R., and Ellis, S. R. (2015) Use of  
675 advantageous, volatile matrices enabled by next-generation high-speed  
676 matrix-assisted laser desorption/ionization time-of-flight imaging employing a  
677 scanning laser beam, *Rapid Communications in Mass Spectrometry* 29, 2195-2203.
- 678 [45] Prentice, B. M., Chumbley, C. W., and Caprioli, R. M. (2016) High-speed MALDI MS/MS  
679 imaging mass spectrometry using continuous raster sampling, *Journal of Mass*  
680 *Spectrometry* 51, 665-665.
- 681 [46] Alonso, A. d. C., Grundke-Iqbal, I., and Iqbal, K. (1996) Alzheimer's disease  
682 hyperphosphorylated tau sequesters normal tau into tangles of filaments and  
683 disassembles microtubules, *Nature medicine* 2, 783-787.
- 684 [47] Hardy, J. A., and Higgins, G. A. (1992) Alzheimer's disease: the amyloid cascade  
685 hypothesis, *Science (New York, N. Y.)* 256, 184-185.
- 686 [48] Yadav, R. S., and Tiwari, N. K. (2014) Lipid integration in neurodegeneration: an  
687 overview of Alzheimer's disease, *Molecular neurobiology* 50, 168-176.
- 688 [49] Hirsch-Reinshagen, V., Burgess, B. L., and Wellington, C. L. (2009) Why lipids are  
689 important for Alzheimer disease?, *Molecular and cellular biochemistry* 326, 121-129.
- 690 [50] Åslund, A., Sigurdson, C. J., Klingstedt, T., Grathwohl, S., Bolmont, T., Dickstein, D. L.,  
691 Glimsdal, E., Prokop, S., Lindgren, M., and Konradsson, P. (2009) Novel pentameric

692 thiophene derivatives for in vitro and in vivo optical imaging of a plethora of protein  
693 aggregates in cerebral amyloidoses, *ACS chemical biology* 4, 673-684.  
694 [51] Han, X., M Holtzman, D., W McKeel, D., Kelley, J., and Morris, J. C. (2002) Substantial  
695 sulfatide deficiency and ceramide elevation in very early Alzheimer's disease:  
696 potential role in disease pathogenesis, *Journal of neurochemistry* 82, 809-818.  
697 [52] Woods, A. S., Colsch, B., Jackson, S. N., Post, J., Baldwin, K., Roux, A., Hoffer, B., Cox,  
698 B. M., Hoffer, M., and Rubovitch, V. (2013) Gangliosides and ceramides change in a  
699 mouse model of blast induced traumatic brain injury, *ACS chemical neuroscience* 4,  
700 594-600.

701

702

## 703 **ASSOCIATED CONTENT**

### 704 **Supporting Information**

705 Supplementary Figure S1- S4, as noted in the text.

706

## 707 **AUTHOR INFORMATION**

### 708 **Corresponding Author**

709 Jörg Hanrieder, PhD

710 Department of Psychiatry and Neurochemistry, Sahlgrenska Academy at the University of  
711 Gothenburg, Mölndal Hospital, House V, Biskopsbogatan 27, SE-43180 Mölndal, Sweden

712 [jh@gu.se](mailto:jh@gu.se); +46-31-343 2377

### 713 **Notes**

714 The authors declare no competing financial interest.

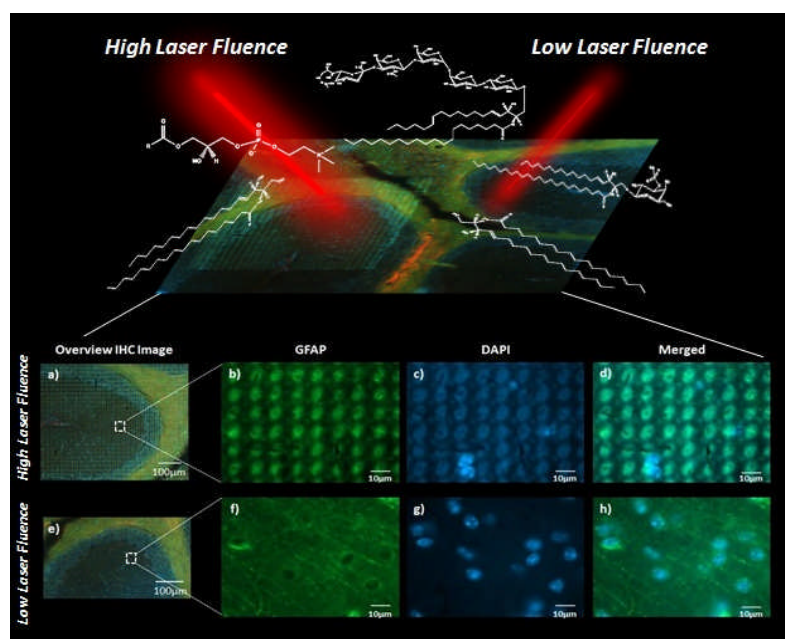
715

## 716 **ACKNOWLEDGEMENTS**

717 The Swedish Research Council VR (#2014-6447, JH; #2012-1593, HZ), the Royal Society of  
718 Arts and Sciences in Gothenburg (KVVS, JH), Alzheimerfonden (JH, KB), Demensfonden  
719 (JH), Hjärnfonden (KB), Jeanssons Stiftelsen (JH), Ahlén Stiftelsen (JH), Stiftelsen Gamla

720 Tjänarinnor (JH, KB), Stohnes Stiftelse (JH) and Stiftelsen Wilhelm och Martina Lundgrens  
721 Vetenskapsfond (JH) are acknowledged for financial support. The work was in part  
722 performed at the goIMS imaging MS infrastructure at the We thank the stuff at Centre for  
723 Cellular Imaging (CCI), Core Facilities, The Sahlgrenska Academy, University of  
724 Gothenburg, in Gothenburg, Sweden. University of Gothenburg ([www.go-ims.gu.se](http://www.go-ims.gu.se)). The  
725 authors declare no conflict of interest.

726 **TOC Figure:**



727